Evolution of crystallographic texture and grain boundary network structure during anisotropic grain growth

José Niño[a,*], Oliver K. Johnson[a]

[a]*Department of Mechanical Engineering, Brigham Young University, Provo, UT 84602, USA*

Abstract

In this paper, we present the results of 426 anisotropic grain growth simulations in two-dimensions using a diverse set of initial microstructures. We consider anisotropy by using a realistic 5D grain boundary (GB) energy function [1]. We sample from the space of all possible crystallographic textures (the texture hull) to generate initial microstructures. The resulting diversity of initial states enables us to evaluate the impact of the initial state on the evolutionary trajectory and identify general trends. We run anisotropic grain growth simulations using these microstructures as the initial points. Additionally, we analyze the evolution of the texture and GB network of these microstructures. We use the orientation distribution function (ODF) and the triple junction distribution (TJD) as the descriptors of the microstructures. We find that at the end of the simulations, there is a universal increase in the sharpness of the ODFs. We identify both a trivial and non-trivial sharpening effect and quantify their contributions to the overall texture sharpening. We also observe a positive correlation between texture strength and its sharpening rate during grain growth. Finally, the evolution of the GB network showed an increase in the low-angle GB fraction in most of the simulations, while spatial correlations in the GB network remained dominated by crystallographic constraints around TJs without the development of longer-range effects.

Keywords: Grain growth, anisotropy, GB network, Texture evolution

1. Introduction

The behavior of polycrystalline materials is dictated, to a significant extent, by their microstructure. Two of the key characteristics of these microstructures are the crystallographic texture and the GB network, whose evolution during grain growth greatly affects the properties of the final microstructure [2]. Hence, gaining an understanding of the influence of the initial microstructure on the final evolved state is vitally important for tailoring material properties to specific needs.

GBs are characterized by five degrees of freedom. Three of these parameters describe the misorientation between two grains, and the remaining two determine the GB plane normal. Traditional grain growth theories assume isotropic conditions [3–5], with numerous simulations conducted based on these assumptions [6–12]. Recent work has increasingly considered more realistic anisotropic GB properties [13–31]. However, a significant portion of anisotropic grain growth studies (e.g., those employing the Read-Shockley model [32]) still consider only the misorientation dependence of GB energy, often neglecting the influence of the GB plane normal.

The development of GB energy databases [33, 34] and advanced energy models [1, 35], has spurred recent anisotropic grain growth studies that account for all five degrees of freedom [28–31]. In our previous work [29], grain growth simulations that

*Corresponding author.
Email address: josens@byu.edu (José Niño)

fully considered anisotropy were executed using an adapted implementation of the level set method by Esedoḡlu [15]. In these simulations, the GB energy model from [1] (referred to as the BRK function) was used to perform these simulations. Two types of microstructure were used to perform the simulations, a microstructure with an initial random texture and a microstructure with an initial fiber texture. While in this previous work, we studied, in-depth and under realistic conditions, the microstructure evolution during grain growth, we only examined a few specific microstructures. As far as we know, a comprehensive survey to understand general trends about microstructure evolution during grain growth across a diverse set of initial microstructural states has not been done yet. Such a study would reveal the influence that the initial state has on the trajectory and rate of microstructure evolution.

In the literature, the ODF has been successfully used as a descriptor of the microstructure [36–38]. While there are experimental studies available [39–41], research on texture evolution during grain growth has predominantly employed statistical modeling and computational simulations [42–46]. These computational simulations have explored various factors influencing the evolution of crystallographic texture. These factors include the initial microstructure (initial texture, grain size distribution), anisotropic GB energy, anisotropic GB mobility, and spatial correlations.

For instance, in [46], they conducted simulations incorporating anisotropic GB energy and isotropic GB mobility on a microstructure characterized by a single texture component within a matrix of random orientations. They observed significant growth in the texture component, even without an initial size advantage for the textured grains. In [42], they studied texture evolution by performing grain growth simulations using a phase field method under different conditions: anisotropic GB energy, anisotropic GB mobility, and both. They found that the primary variable that influences texture evolution is the GB energy density. For their simulations, they used a microstructure with an initial ODF composed of a single cube component (assigned to 27% of grains) in a matrix of random orientations. More recently, Zollner [43] performed simulations with anisotropic GB energy and mobility. They examined three different initial microstructures: one with a primary high-angle misorientation distribution function (MDF), another with a uniform MDF, and a third with a low-angle MDF. They discovered that in the first scenario, the microstructure evolved ideally, while in the latter two scenarios, the microstructure tended to preserve and augment the fraction of low-angle GBs.

Additionally, the evolution of the triple junction distribution serves as a key descriptor of the GB network. In previous work [47], Lu and Yang generated and analyzed polycrystals with random orientations and various texture intensities defined by fractions of Goss orientation. They found that in microstructures with stronger textures, the triple junctions had more special boundaries. Lastly, it's worth mentioning that all these studies on grain growth with different GB energies used a GB energy function that only considers the misorientations between grains.

The *texture hull* represents all possible crystallographic textures a given material can adopt [48]. By systematically sampling initial microstructures from the texture hull, it is possible to explore a broad range of initial conditions and observe how they evolve under grain growth. The texture hull has been explored to study texture evolution during strain hardening [49] and deformation processing [50, 51]. In addition, Johnson et al. [52] recently developed an algorithm to generate ODFs that explore the texture hull more efficiently.

The primary focus of this study is to investigate the role of the initial crystallographic texture on the final evolved state by considering a comprehensive set of initial ODFs. We generated this set of initial ODFs by sampling from the texture hull using the algorithm outlined in [52]. Then, we sampled orientations from the ODFs and assigned them uniformly at random to grains in each 2D microstructure. This implies that there were no spatial correlations in grain orientation in the initial states. Such an absence of spatial correlations occurs in real materials under certain processing conditions such as powder metallurgy [53], rapid solidification [54], or mechanical alloying [55]. Each

of the initial microstructures was subsequently subjected to anisotropic grain growth simulations using the level-set methods explained in [29]. Finally, we monitored the evolution of the ODFs and visualized their respective trajectories within the texture hull. In addition, we explored whether different initial microstructures evolve separately or if they converge towards a common texture. This aspect has relevance for materials design, potentially providing a roadmap to tailor the properties of polycrystalline materials based on their initial texture.

In Section 2.1, we detail the methodology employed to generate the set of initial ODFs spanning the texture hull. Our visualization techniques for representing ODFs within the texture hull are elaborated in Section 2.2. The grain growth simulation approach, along with the associated parameters, is delineated in Section 2.4. Section 3 provides an overview of the grain growth simulation outcomes, including charting the trajectory of ODFs within the texture hull. In Section 4, we discuss the evolutionary patterns of diverse ODFs, especially contrasting those with strong and weak textures. Our findings and their implications are summarized in Section 5.

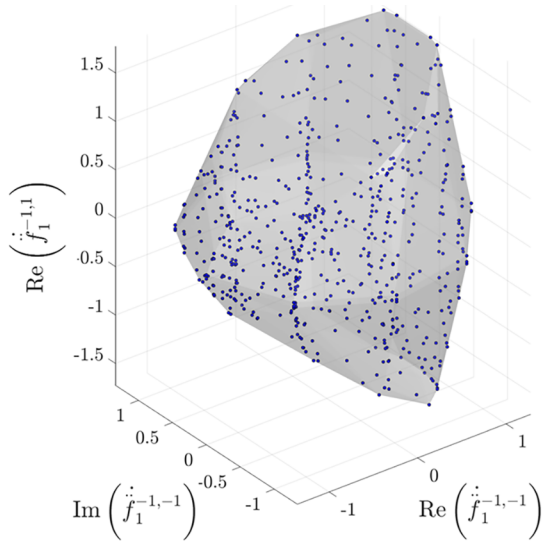

Figure 1: The texture set (the Fourier coefficients of the fundamental ODFs) visualized in a 3D orthogonal projection.

2. Methods

2.1. ODF Generation

To generate a diverse set of ODFs, we first construct the texture hull, and then we sample ODFs from it. Construction of the texture hull involves the following steps:

1. **Obtain fundamental orientations:** The cubic orientation fundamental zone (FZ) is a region in orientation space where each point represents a unique orientation. We sample orientations uniformly over the cubic orientation fundamental zone (FZ). These are referred to as "fundamental orientations" [56, 57]. We used MTEX [58] to define equispaced points in the FZ. The cubic orientation FZ was discretized with a resolution of 10°, resulting in K = 618 fundamental orientations: $\{g_k \mid k \in [1, K]\}$.
2. **Define the texture set:** We first associate a Dirac delta function ODF with each fundamental orientation,

$$f_k(g) = \delta(g, g_k)\,. \tag{1}$$

We then employ a finite harmonic expansion approximation of each fundamental ODF:

$$f_k(g) = \sum_{s=0}^{S} \sum_{\mu=1}^{M(s)} \sum_{\nu=1}^{N(s)} \dot{\ddot{f}}_s^{\mu\nu} \ddot{D}_s^{\mu\nu}(g)\,, \tag{2}$$

with $S = 32$ and where $\dot{\ddot{f}}_s^{\mu\nu}$ are the complex Fourier coefficients and $\ddot{D}_s^{\mu\nu}$ are the basis functions. The $\ddot{D}_s^{\mu\nu}$ are a variation of the Wigner-D functions as defined in MTEX (see [59]), symmetrized for O_h crystal symmetry and triclinic sample symmetry (see [38]). The Fourier coefficients of a particular ODF constitute coordinates in this 3,988-dimensional vector space[1]. Thus, each ODF can be represented by a point in this space. The set of Fourier coefficients

[1]There are 1,994 complex coefficients for O_h point group symmetry and $S = 32$, resulting in a real vector space with $2 \times 1{,}994 = 3{,}988$ dimensions due to the real and imaginary components each coefficient.

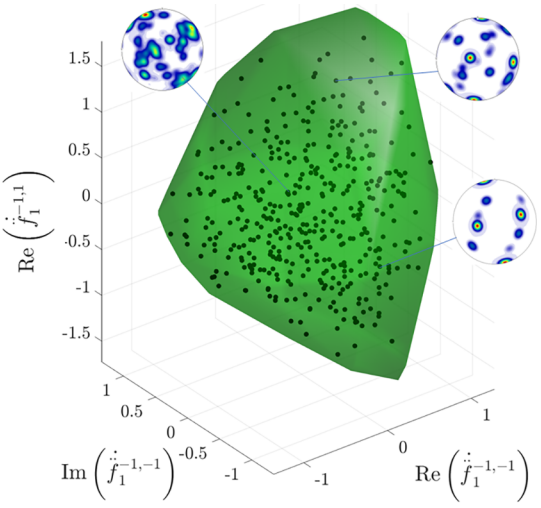

Figure 2: The texture hull together with points representing the 426 ODFs used in this study. (001) Pole figures corresponding to a few representative points are also illustrated.

for all fundamental ODFs is convex and constitutes the texture set, as shown in Fig. 1.

3. **Define the texture hull:** The texture hull (see Fig. 2) is simply the convex hull of the texture set [56]. It is closed, compact, and obviously convex. Any ODF can be represented as a point contained in the texture hull whose coordinates are given by its Fourier coefficients, which can, themselves, be expressed as a linear combination of the Fourier coefficients of the fundamental ODFs [60].

Having defined the texture hull, which contains all possible ODFs (under a particular discretization of SO(3)), we proceed to sample ODFs from it by means of the hierarchical simplex sampling (HSS) algorithm [52], which promotes uniform sampling of both the interior and surface of the texture hull. After sampling, the coefficients are adjusted by a convergence acceleration technique [61] to ensure non-negativity of the resulting ODF (eliminating truncation artifacts from the fact that S is finite).

2.2. ODF Visualization in the Texture Hull

The texture hull resides in a high-dimensional space, causing a full visualization of the Fourier coordinates of each ODF and their subsequent evolution to be unattainable. We have chosen to display the texture hull and the evolution trajectories of the ODFs by orthogonal projection in the first 3 non-trivial dimensions. Fig. 1 displays the texture set and Fig. 2 shows the texture hull.

Following the construction of the texture hull, as referenced in Section 2.1, we uniformly dispersed a sample of 10,000 ODFs throughout its multi-dimensional space. Although the 10,000 points are well distributed in the full 3,988-dimensional space, in the 3D projection used for visualization, points appear congregated near the origin. Thus, for ease of visualization and to ensure comprehensive coverage of the texture hull (visualized in Fig. 2), we partitioned it into 1,000 equally-sized bins. From our initial 10,000 ODFs, we then chose a representative point within each bin. Given that certain bins didn't contain any points, our final selection culminated in 426 distinct points. These specific 426 points, which span the 3D projection of the texture hull, were subsequently employed as the initial ODFs for our grain growth simulation microstructures.

2.3. Initial Microstructures

We use a similar procedure employed in our earlier work [29] to define the initial microstructures. This includes starting with a two-dimensional Voronoi tessellation containing 10,000 grains. After constructing the microstructural template, we assigned a crystallographic orientation to each initial grain. The orientations were sampled from the ODFs generated in Section 2.1 using MTEX [62]. In all cases, the orientations sampled from the respective ODFs were subsequently assigned to grains in the microstructure template uniformly at random. Assigning grain orientations directly ensures that crystallographic constraints are satisfied by construction. The process to generate the initial microstructures is summarized in Fig. 3. Additionally, Fig. 4.(a)-(d) shows four samples of initial microstructures created following this process.

2.4. Anisotropic Grain Growth Simulations

The fully anisotropic grain growth simulations were performed using the methods from our prior work [29], which are an extension of the level set method developed by Esedoğlu [15], based on one of the algorithms described in [15] with adaptations

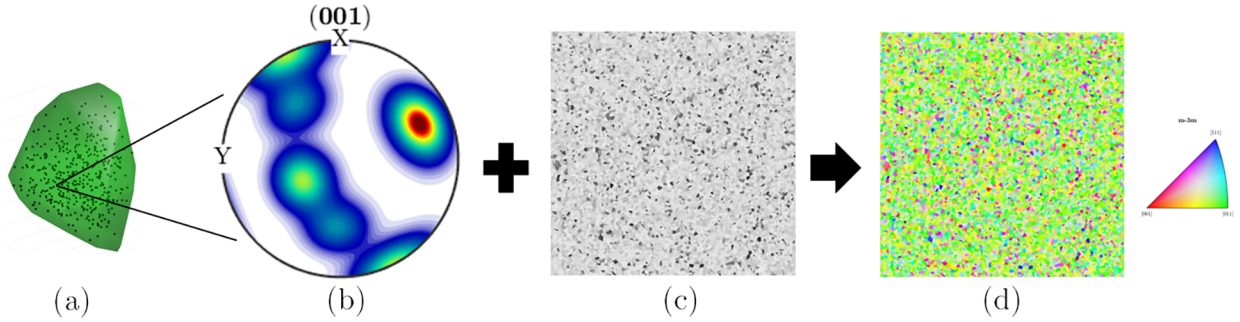

Figure 3: (a) Texture hull with the 426 ODFs (black points). (b) Pole figure of one of the ODFs sampled from the texture hull (generated using MTEX [62]). (c) Microstructure template from Voronoi tessellation containing 10,000 initial grains. (d) Initial state of a microstructure for grain growth simulations after assigning orientations sampled from the ODF.

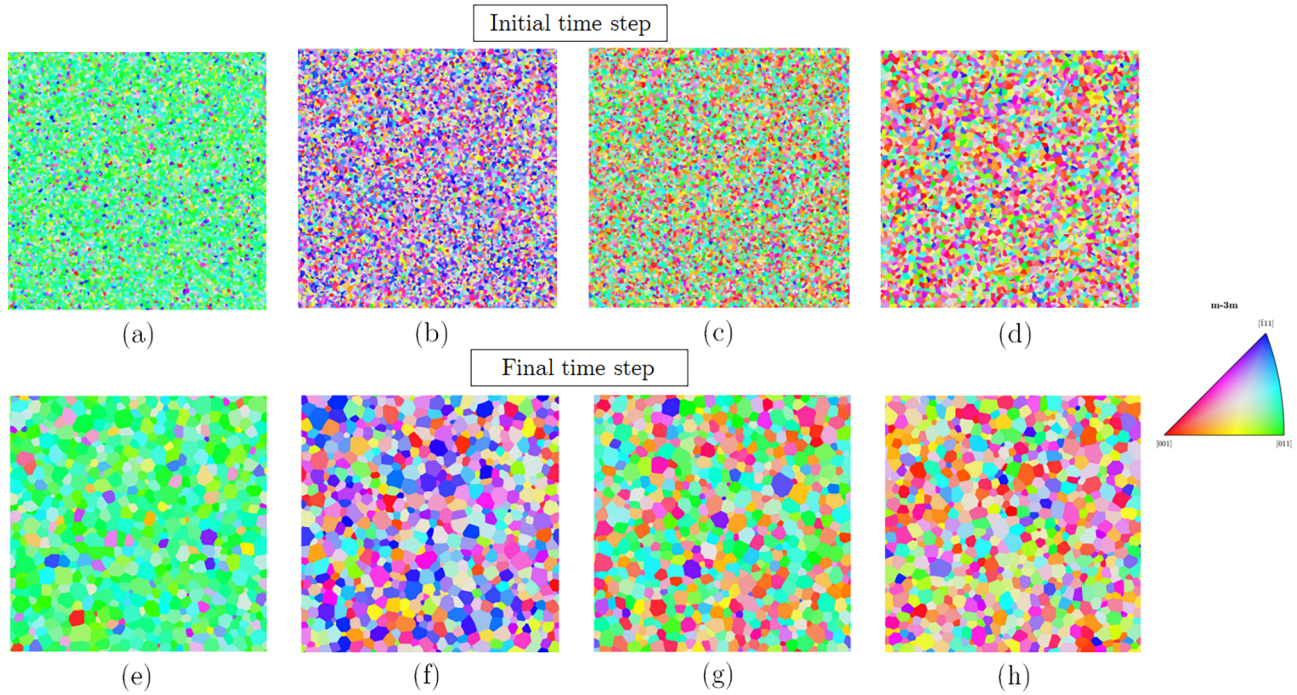

Figure 4: (a)-(d) Four initial microstructures (10,000 grains) and (e)-(h) the corresponding final microstructures (∼700 grains) from the 426 anisotropic grain growth simulations. Grain colors and corresponding color legend were constructed using MTEX [62].

to employ the fully anisotropic 5D BRK GB energy model [1]. The material simulated in the energy function was nickel (Ni).

The algorithm simulates the mean curvature motion of networks of interfaces under arbitrary GB energies. Classical theories consider that the local velocity of a GB is proportional to its local curvature (κ), and it is determined by the equation:

$$v = M\gamma\kappa \tag{3}$$

where M is the GB mobility, and γ is the GB energy. In this version of Esedoḡlu's MATLAB implementation of the level-set method $v = \kappa$ which implies that $M\gamma = 1$. As a result, the simulations do not capture independent mobility effects (though the effect of mobility is expected to be small compared to the effect of the GB energy [22, 23]). Even though M and γ cancel out, the GB energy anisotropy still controls the GB motion. This is because the curvature of any given boundary is determined by conditions of force equilibrium at its terminating triple junctions (the Herring condition [63]). The simulation methodology employed here

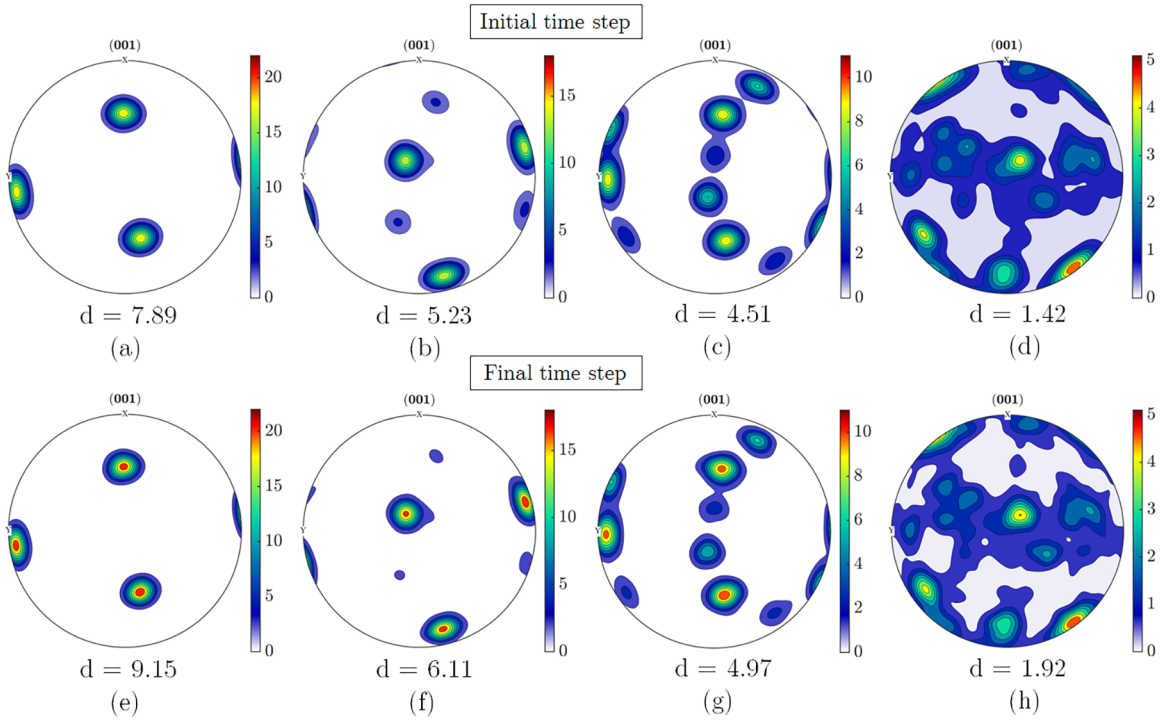

Figure 5: (a)-(d) Initial and (e)-(h) final ODFs corresponding to the microstructures shown in Fig. 4. The distance from the origin of the texture hull is indicated for each.

has been confirmed to enforce/satisfy these equilibrium conditions [15, 29]. The anisotropic GB energy determines the dihedral angles at each triple junction, which determine the curvature of each GB, and consequently their velocity.

Using this procedure, each of the 426 initial microstructures was subjected to anisotropic grain growth. Each simulation was run for 800 time steps with a step size of $\Delta t = 3 \times 10^{-6}$. The state of the microstructure was saved every 30 time steps. At the end of the simulations, the microstructures had less than 10% of the grains remaining (around 700 grains).

Fig. 4(e)-(h) displays the concluding evolved states of four microstructures from the simulations. After performing the simulations, we obtained a large dataset of 426 microstructures across 121 time steps each, for a total of 51,546 microstructural states.

Every microstructure was stored as an 800×800 label matrix, where the label in a given pixel indicates the grain orientation at that point from the accompanying list of initial orientations (represented as quaternions) assigned to each grain. The data acquired from each grain growth simulation is accessible in [dataset] [64].

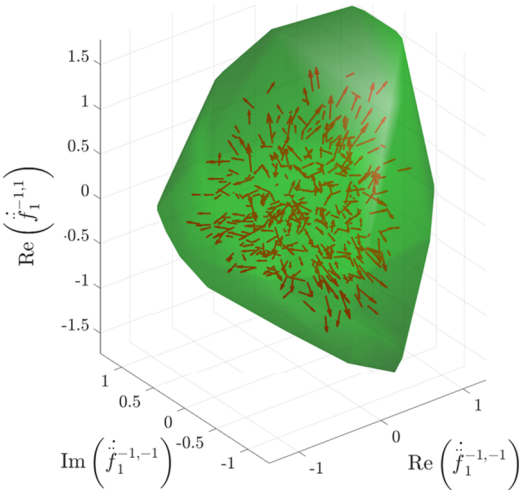

Figure 6: The texture hull and arrows representing the trajectory of the 426 ODFs during the simulations.

3. Results

3.1. ODF Evolution

In Fig. 6, we can see the trajectory of the 426 ODFs during the simulations. Each ODF is repre-

sented by an arrow that goes from the initial ODF to the final ODF. The arrows tend to point away from the texture hull's origin. The relative position of an ODF to the texture hull's origin is an indicator of its randomness. ODFs proximate to the origin have a random texture. In contrast, ODFs located farther from the origin present a stronger texture. The range of distances to the origin in the generated 426 ODFs is 0.7 to 9.4. Beyond this range, the textures are so sharp that they are essentially single crystals. These distances were calculated using all 1,994 of the complex valued coefficients (not just the 3 used for visualization in Figs. 1–3 and 6).

Fig. 5.(a)-(d) shows four initial ODFs (out of the 426) chosen for their varying distances from the origin of the texture hull. The corresponding evolved ODFs are illustrated in Fig. 5.(e)-(h). Both initial and final ODFs maintain similar overall shapes, and textures seem to get sharper for ODFs with strong initial textures (e.g., Fig. 5.(a)). However, we don't see as pronounced of a change in texture for the ODFs that started with a weak texture (e.g., Fig. 5.(d)).

Moreover, to visualize the change in the distance between all the ODFs to the origin, Fig. 7 illustrates the distribution of these distances for the initial and final state of the ODFs. Notably, a discernible shift to the right in the final ODF distribution is evident. Quantitatively, the average distance for initial ODFs is 4.91, while the post-simulation ODFs present an average of 5.60. The difference is a 14.03% increase in distance, which is significant and highlights the ODF evolution during grain growth.

While the accumulated distances between ODF points and the origin suggest an increase for the evolved states, it's important to determine whether this trend is universal or limited to a subset of the initial ODFs. To estimate the trajectory of each point in the texture hull relative to the origin, Fig. 8 displays the extent of displacement each ODF underwent during the simulations. Notably, all recorded distances were positive, signifying that *every* ODF moved further from the origin as the simulation progressed. Since closeness to the origin denotes a random texture, this pattern suggests that all textures get sharper during anisotropic grain growth.

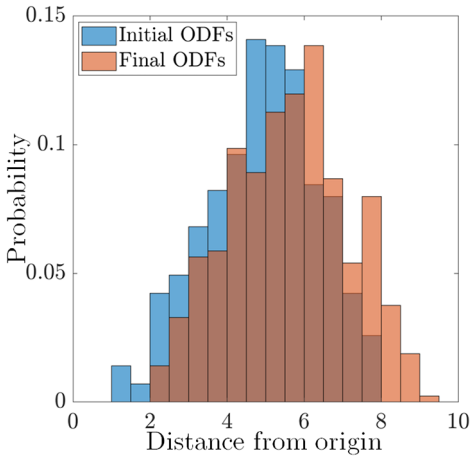

Figure 7: Distribution of the distance from the origin before and after anisotropic grain growth.

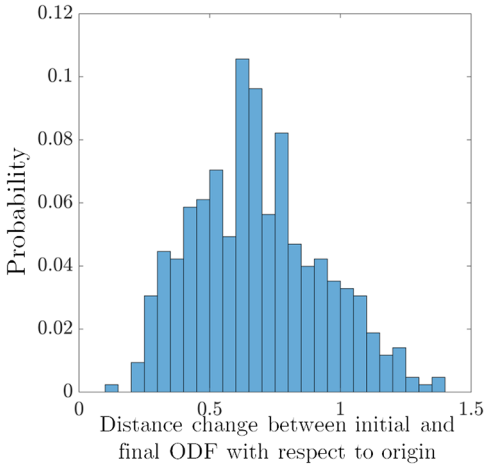

Figure 8: Distribution of the change in the distance from the origin after anisotropic grain growth.

3.2. TJD Evolution

In this section, we present the results of the TJD's evolution throughout the grain growth simulations. The term (J_i) represents the triple junction fractions, designating the fraction of TJs in the microstructure coordinated by i low-angle GBs (LAGBs). The array $[J_0, J_1, J_2, J_3]$ is commonly referred to as the TJ Distribution (TJD).

Our simulations show distinct evolutionary trends in the TJD across two microstructure types. The TJD at each time step are plotted for a representative microstructure of each type in Fig. 9.

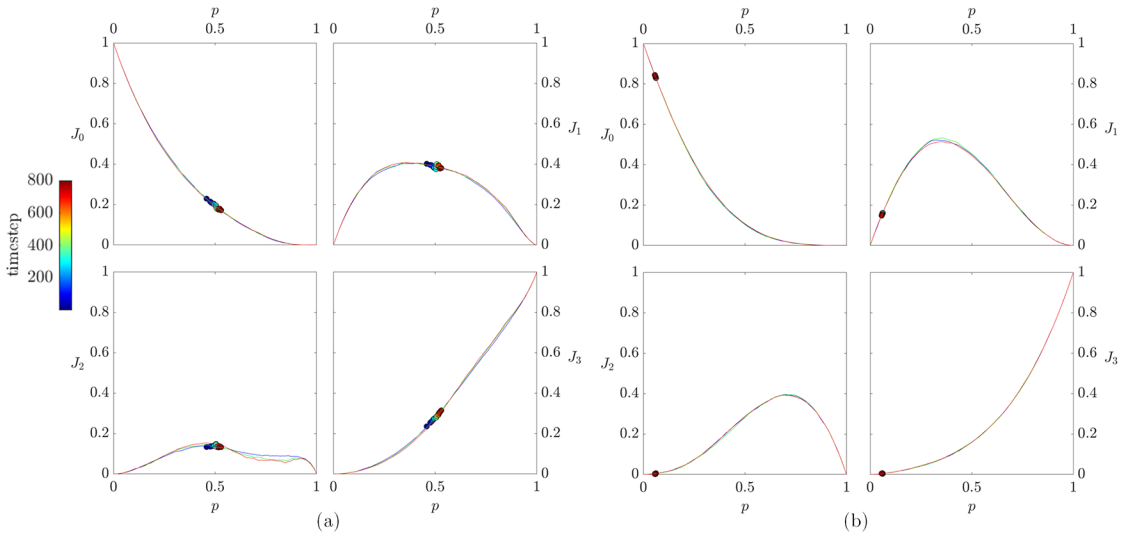

Figure 9: TJD evolution of a microstructure with (a) strong texture and (b) weak texture. Solid lines show the uncorrelated TJD predicted for the ODF at each of the respective time steps: initial (blue), intermediate (green), and final (red).

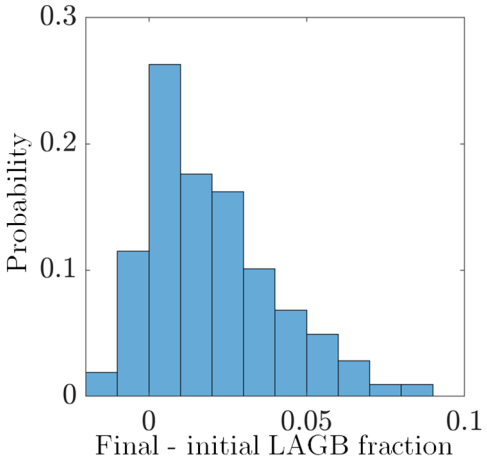

Figure 10: Distribution of change in LAGB fractions (p).

First, Fig. 9.(a) illustrates the evolution of a microstructure exhibiting strong texture, with an initial ODF from Fig. 5.(a). In Fig. 9, p represents the length-fraction of LAGBs, applying the conventional 15° threshold. Here, the value of p increased from 0.4583 to 0.5302 throughout the simulations. Accordingly, there is a trend of decreasing J_0, slightly decreasing J_1, and increasing J_3, whereas J_2 remains largely unchanged. The diminution in J_0 and increase in J_3 show that there is an increase in connections between LAGBs and a decrease in connections between high-angle GBs (HAGBs). In addition, initial TJ fractions do not deviate from the uncorrelated TJD [65–67] (illustrated by the solid lines and defined in Section 4.4). Moreover, it is evident that J_0 and J_3 fall on top of the uncorrelated lines, while J_1 and J_2 stay close to the uncorrelated lines but slightly deviate from them at some time steps. Other simulations with initial microstructures with moderate to strong textures presented similar behavioral traits.

Conversely, the evolution of the TJD for weak texture microstructures (ODF from Fig. 5.d) is illustrated in Fig. 9.(b). The LAGB fraction p remains relatively stagnant throughout the simulations. Initially, the TJs are predominantly J_0-type. However, no significant transformation is observed in the values of the J_i. Additionally, in this case, the TJ fractions stay in proximity to the uncorrelated TJD (they fall on the red line).

In Fig. 10, we can see the change of the LAGB fractions for each microstructure. Positive values mean that the LAGB fraction increased. Most of the microstructures have a positive difference. There are some microstructures that have a negative change. However, these instances where the LAGB fraction decreases are small in magnitude (close to zero), which suggests that for such cases, the LAGB fraction value didn't change significantly during the simulations.

The mean LAGB fraction value for all the initial microstructures stands at 0.20, while the final average increases slightly to 0.22. This represents a

10.47% difference, presenting a general trend: the proportion of LAGBs tends to increase as the microstructures evolve.

4. Discussion

As is apparent from the foregoing results, texture appears to universally sharpen during grain growth. In addition, we observe that microstructures with a stronger initial texture show a larger change during grain growth. In this section, we explore possible explanations for these observations.

It is noteworthy that grain growth is governed by the principle of minimization of the total energy in the system. One of the mechanisms to minimize the system's energy is by expanding the size of low-energy GBs at the expense of high-energy GBs by the motion of triple junctions. This mechanism is relevant in our simulations as we consider anisotropic GB energy.

To explain how the microstructure gets sharper, let us consider a simulation where the microstructure (e.g., Fig. 5.(a)) contains one predominant orientation, q, while the rest are random orientations r. When the proportion of orientation q dominates, there is a high proportion of low-angle GBs (q-q boundaries) compared to high-angle GBs (q-r or r-r boundaries). Consequently, q-q boundaries are low-energy GBs, and q-r or r-r boundaries are likely high-energy GBs. During grain growth, at each triple junction, the high-energy GBs tend to reduce in size and eventually disappear, preserving the low-energy GBs. Thus, grains separated by low-energy (primarily low-angle) GBs are more likely to persist, whereas grains separated by high-energy GBs are more likely to be the ones that get eliminated, leading to a more pronounced texture in the microstructure. For example, Fig. 11 shows a grain that persisted in one of the simulations. In the initial microstructure, this grain had an average disorientation angle of 14.57, while it ended with a disorientation angle of 11.39. Similar to this grain, most grains in the last simulation step present a lower disorientation angle than at the beginning of the simulation. However, the survival or disappearance of grains is influenced by various factors, including but not limited to grain size and spatial correlations. While the presence of low-angle grain boundaries (LAGBs) may contribute to a grain's persistence, it could still disappear due to other factors.

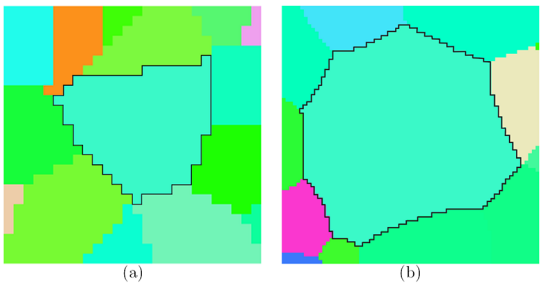

Figure 11: (a) Grain at the first time step of the simulation. (b) The same grain at the last time step of the simulation.

Experimental investigations have also observed texture enhancement during texture evolution. For instance, in the experiments reported by [68], the annealing of a rolled magnesium alloy resulted in a significant sharpening of the texture. They hypothesized that the anisotropic GB properties are responsible for the strengthening of the texture. Moreover, experiments have also reported an increase in the fraction of LAGBs during grain growth [24, 40]. Specifically, Gruber et al. [24] analyzed polycrystalline magnesia samples and measured the misorientation distribution function. Their findings showed that there was an increase in the average area of LAGBs during the experiment. These results are consistent with our observations in the present work.

This texture enhancement, along with the rise in LAGBs, is reflected in the TJD's evolution. The data indicates a growing fraction of LAGBs, which correlates with the decline in J_0 and the surge in J_3. As the microstructure progresses, the diminishing HAGBs make triple junctions dominated by three HAGBs less frequent, favoring those where all GBs are LAGBs. It is apparent that during this evolution, triple junctions transition from J_0 to J_3. In this transformation, they might temporarily shift to J_1 or J_2, serving as transitional states.

Although all textures become sharper during the simulations, the extent of this change varied depending on the specific ODF. Even though most GB networks increased the LAGB fraction, the

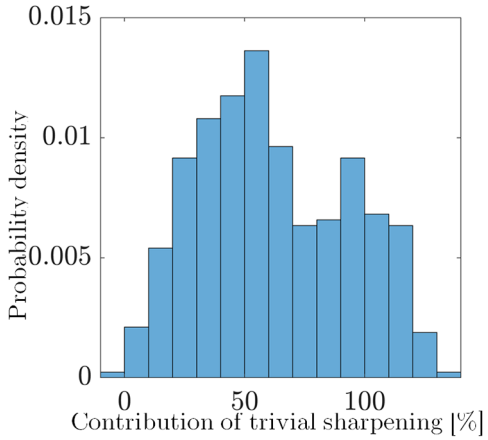

Figure 12: Distribution of the contribution of trivial sharpening (percent of total sharpening).

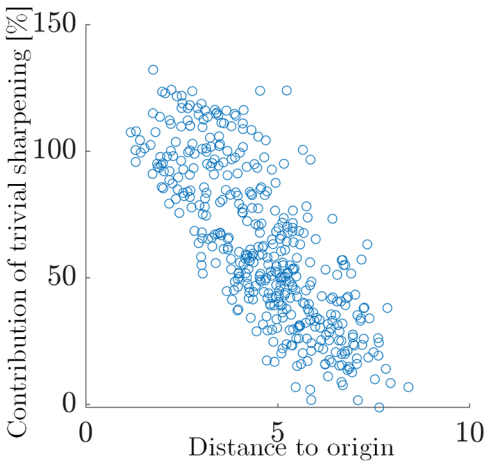

Figure 13: Scatter plot of the ODF's initial distance to the origin vs. Contribution from trivial sharpening.

magnitude of this increase differed across the various microstructures. In the following subsections, we discuss and analyze the type of microstructures that present a larger and smaller change during grain growth. We also analyze possible causes for these changes. In addition, we discuss changes in the ODF beyond just sharpness.

4.1. Trivial vs non-trivial sharpening

We have observed the sharpening of the ODFs during grain growth and analyzed how minimizing energy during grain growth could lead to this sharpening. However, there are potentially two distinct sources of texture sharpening. The first is the trivial source: as grain growth proceeds, there are fewer grains, and with fewer grains, the texture necessarily sharpens. The second is the non-trivial sharpening that we discussed previously.

To test whether the sharpening experienced by the ODFs comes from the trivial or the non-trivial source, we calculate the contribution of the trivial effect to the total texture sharpening in each microstructure. To calculate the trivial sharpening, we start with the initial set of grains of a microstructure and the corresponding orientations. We randomly pick a subset from this set of grains. The subset has the same size as the number of grains in the final time step for that microstructure. Then, using the subset of grain orientations, we generate an ODF and calculate its distance to the origin in the texture hull. The difference between this distance and the distance of the initial ODF from the origin is an estimate of the amount of trivial sharpening as it comes from down-sampling the initial ODF. Finally, we calculate the percentage of trivial sharpening by taking the ratio of the trivial change in distance to the actual change in distance. We repeated this process 100 times for each ODF and took the average as an estimate of the amount of trivial sharpening.

Fig. 12 shows the trivial sharpening percentage distribution for all ODFs. As expected, the trivial sharpening is positive or close to zero for all the ODFs. The range of trivial sharpening percentage is 0% to 151%. Percentages above 100% mean that for those ODFs, the total traveled distance is less than the trivial sharpening estimate. Most percentages are under 100%, but as some distances traveled were minor, even small differences with the trivial sharpening estimate could mean high percentages.

Additionally, Fig. 13 presents the correlation between the initial distance to the origin and the degree of trivial sharpening percentage. There is a strong negative Pearson's correlation with a coefficient $\rho_P = -0.78$. This correlation shows that while all ODFs experienced some trivial sharpening (as expected), the magnitude of this sharpening varied among them. ODFs that present a weaker texture exhibited a more substantial degree of trivial sharpening compared to those with a stronger texture. For a weak texture ODF (like Fig. 5.(d)), trivial sharpening is around 91.52% of the total sharpening, while for a microstructure

with a strong texture (Fig. 5.(a)), trivial sharpening represents only 8.67% of the total sharpening. This is significant because it indicates that strong textures not only experience a large degree of sharpening, but nearly all of that sharpening is due to the non-trivial effect caused by the GB energy anisotropy.

4.2. ODF Randomness and Evolution Rate Correlation

We further analyze which initial ODFs underwent significant changes and which ones remained relatively stable. In Fig. 14, we plot the distance each ODF moved relative to the origin of the texture hull against their starting distance from the origin. Our data revealed a moderate positive correlation, with a Pearson's correlation coefficient of $\rho_P = 0.47$. This suggests a weak relationship, accounting for 22% of the shared variance ($R^2 = 0.22$).

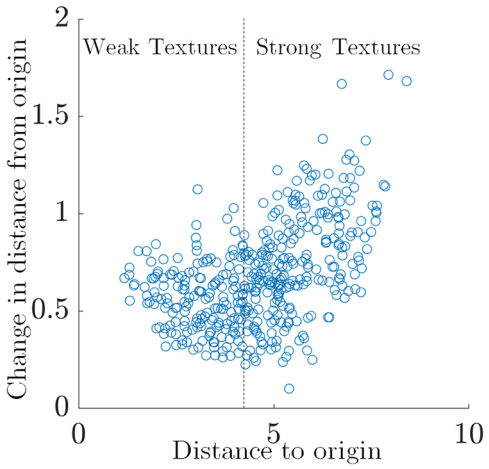

Figure 14: Scatter plot of distance between ODF from origin vs. Difference between initial and final ODF with respect to the origin.

However, a closer look at Fig. 14 suggests the presence of two separate distributions. The first set of data points, with initial distances ranging from 0 to 4.31, differs from the second set, spanning distances from 4.31 to 10. Breaking these groups apart for further analysis, we found that the first group, associated with weak texture, had a Pearson's correlation of $\rho_P = -0.16$ (essentially a negligible relationship). In contrast, the second group, corresponding to strong-textured ODFs, exhibited a more robust correlation of $\rho_P = 0.54$, which is a stronger correlation when compared to the entire dataset's correlation. This indicates that weak textures remain largely static, while stronger textures sharpen during grain growth. Moreover, on average, the sharper the initial texture, the faster the rate of sharpening.

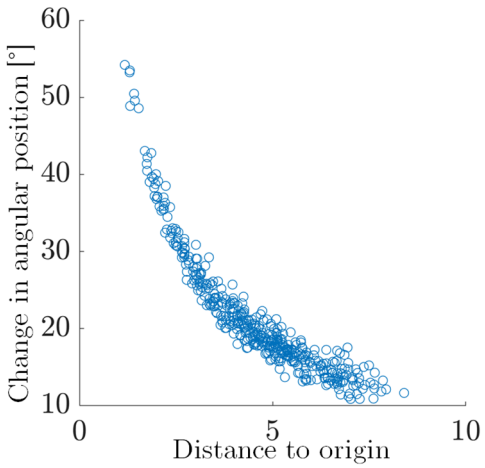

Figure 15: Scatter plot of the ODF's distance to the origin vs. Change in angular position between initial and final ODF.

4.3. ODF Reshaping/Rotation

Up to this point, we have analyzed the change in the radial position of the ODFs within the texture hull. In this section, we examine changes in the angular position. An ODF that exhibits positive radial movement without any angular change means that the ODF presents essentially the same shape and is only getting sharper. In contrast, changes to the angular position of an ODF in the Fourier space represent rotations or changes in the shape of the ODF. An evolutionary trajectory that has no radial component signifies that the ODF has rotated or morphed so that probability density has shifted to different orientations.

To evaluate the change in the angular position of each simulation, we construct two vectors. The first vector goes from the origin to the initial ODF in the texture hull, and the second vector goes from the origin to the final ODF (using all of the coefficients in both cases). The angle between these two vectors represents the angular change of the ODF.

In Fig. 15, we can see the relationship between

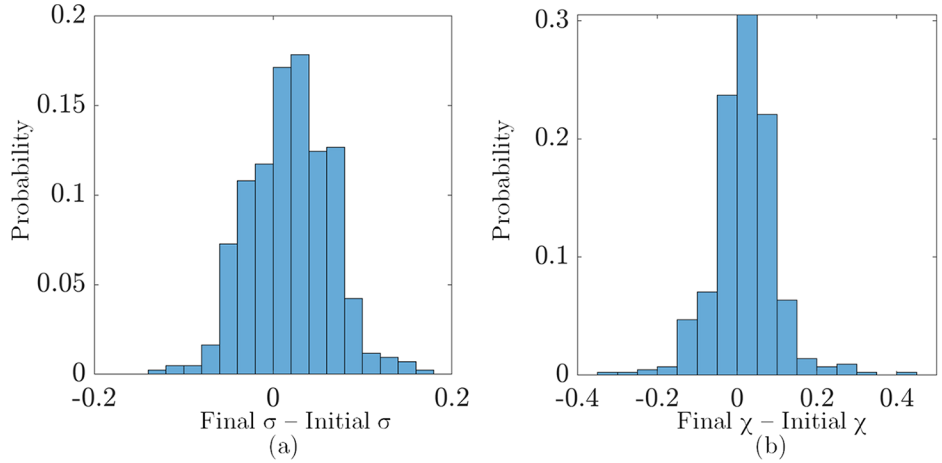

Figure 16: Difference between initial and final order parameters (a)χ and (b) σ.

the change in angular position and the initial distance to the origin for each ODF. The data exhibits a very strong negative Spearman's correlation with a coefficient of $\rho_S = -0.93$. The microstructures with a more random texture (smaller distance from the origin) present a large change in angular position. And the microstructures with a strong texture show a smaller angular movement.

This observation suggests that ODFs with a weak texture do not develop a texture but rather undergo rotations or morphological changes in their ODF. For these microstructures, as there are no predominant orientations, grain size fluctuations and disappearing grains during grain growth may cause significant rotations or morphological changes to the ODF. On the other hand, for ODFs with a strong texture, grain growth does not induce changes to the angular position of the ODF, but only results in sharpening of the ODF (radial motion). Thus, there appear to be two fundamentally different evolutionary trajectories of texture during grain growth depending on the initial state.

4.4. GB network evolution

Fig. 16 shows the change of the GB network topological order parameters [65]. χ, represents the tendency of LAGBs to form either compact ($\chi < 0$) or elongated ($\chi > 0$) clusters, and σ, indicates the tendency of LAGBs and HAGBs to mix ($\sigma < 0$) or phase separate ($\sigma > 0$).

While some GBNs experience a slight increase in χ and others a slight decrease, on average, there is no significant change χ between the initial and final states. On the other hand, there is a slight increase in σ on average, which indicates a preference for phase separation of the LAGBs and HAGBs. However, the change in σ is also negative for some microstructures, and the average increase is small.

Additionally, we analyze the strength of correlations in the evolution of the GB network. The TJ fractions are a measure of the type and strength of local correlations in GB type around TJs. The uncorrelated TJD [65, 66, 69] describes the distribution of triple junctions at each fraction of LAGBs in the absence of spatial correlations in grain orientation. In Fig. 9.(b), the TJD matches the uncorrelated predictions (for each particular texture). This indicates that the short-range correlations required by crystallographic constraints around TJs dominate throughout the grain growth process without the development of significant longer-range correlations in the GB network. For strong texture ODFs, in Fig. 9.(a), the result is similar, but the TJD deviates slightly from the uncorrelated lines for J_2 and J_3. Thus, in all cases, the observed evolution in the TJD (which we use as a descriptor of the GB network structure) can be explained almost entirely by the increase in LAGBs, without the emergence of any longer-range correlations.

5. Conclusion

In this research, we generated a set of 426 ODFs, spanning the texture hull. Using this extensive

set of ODFs, we constructed initial microstructures that we used to perform a broad survey of fully anisotropic (5D GB energy model) grain growth simulations on 2D microstructures. The primary objective of our study was to investigate how the initial state of the microstructure influences its evolution and make general observations. Our key findings include:

- As the simulations advanced, all ODFs got sharper during grain growth. On average, the distance from the uniform ODF increased by 14.03%, but ranged from 1.60% to 57.63% depending on the initial state.

- We distinguished between trivial sharpening due to the disappearance of grains (coarsening of the microstructure) and a novel non-trivial texture sharpening effect. We proposed a mechanism to explain this non-trivial sharpening effect (which is caused by GB energy anisotropy) and quantified its influence relative to trivial sharpening. We found that weak textures sharpen very little and any sharpening that does occur is primarily due to the trivial effect. In contrast, stronger textures sharpen significantly, and that sharpening is primarily due to the non-trivial effect.

- We found that the evolutionary trajectory of weak textures during grain growth is primarily rotation or a change in the shape of the ODF, while the trajectory of strong textures is primarily sharpening while preserving the shape of the ODF and the locations of its peaks.

- Our analysis showed a significant positive correlation between texture strength and its transformation *rate* during grain growth. This suggests that the stronger the initial texture, the faster the sharpening of the ODF.

- Analysis of the GB network evolution revealed that the low-angle GB (LAGB) fraction consistently increased, with an average increase of 10.47% over the duration of the simulations. While the structure of the GB network did evolve (increase in J_1, J_2, and J_3 and decrease in J_0), this evolution can be explained almost entirely by the increase in the LAGB fraction without the emergence of any correlations beyond the local constraints of crystallographic consistency around TJs.

Acknowledgement

The material presented here is based upon work supported by the National Science Foundation under Grant No. 1654700. This work was supported in part through computational resources provided by Brigham Young University's Office of Research Computing.

6. Data availability

Supplementary data associated with this article can be found in Mendeley data [64].

References

[1] V. V. Bulatov, B. W. Reed, M. Kumar, Grain boundary energy function for fcc metals, Acta Materialia 65 (February) (2014) 161–175. doi:10.1016/j.actamat.2013.10.057. URL http://dx.doi.org/10.1016/j.actamat.2013.10.057

[2] G. Gottstein, L. S. Shvindlerman, Grain Boundary Migration in Metals., 2010, thermodynamics, Kinetics, Applications, Second Edition. doi:https://doi.org/10.1201/9781420054361.

[3] W. W. Mullins, Two-dimensional motion of idealized grain boundaries, Journal of Applied Physics 27 (8) (1956) 900–904. doi:10.1063/1.1722511.

[4] J. von Neumann, Seminar Report (Cleveland, Ohio: American Society for Metals) (1952).

[5] R. D. MacPherson, D. J. Srolovitz, The von Neumann relation generalized to coarsening of three-dimensional microstructures, Nature 446 (7139) (2007) 1053–1055. arXiv:t8jd4qr3m, doi:10.1038/nature05745.

[6] F. Wakai, N. Enomoto, H. Ogawa, Three-dimensional microstructural evolution in ideal grain growth general statistics, Acta Materialia 48 (6) (2000) 1297–1311. doi:10.1016/S1359-6454(99)00405-X.

[7] E. A. Lazar, R. D. Macpherson, D. J. Srolovitz, A more accurate two-dimensional grain growth algorithm, Acta Materialia 58 (2) (2010) 364–372. doi:10.1016/j.actamat.2009.09.008.
URL http://dx.doi.org/10.1016/j.actamat.2009.09.008

[8] E. A. Lazar, J. K. Mason, R. D. Macpherson, D. J. Srolovitz, A more accurate three-dimensional grain growth algorithm, Acta Materialia 59 (17) (2011) 6837–6847. doi:10.1016/j.actamat.2011.07.052.
URL http://dx.doi.org/10.1016/j.actamat.2011.07.052

[9] A. Kuprat, D. George, G. Straub, M. C. Demirel, Modeling microstructure evolution in three dimensions with Grain3D and LaGriT, Computational Materials Science 28 (2) (2003) 199–208. doi:10.1016/S0927-0256(03)00107-1.

[10] A. L. Cruz-Fabiano, R. Logé, M. Bernacki, Assessment of simplified 2D grain growth models from numerical experiments based on a level set framework, Computational Materials Science 92 (2014) 305–312. doi:10.1016/j.commatsci.2014.05.060.
URL http://dx.doi.org/10.1016/j.commatsci.2014.05.060

[11] M. Elsey, S. Esedo, P. Smereka, Large Scale Simulations and Parameter Study for a Simple Recrystallization Model, Philosophical Magazine (2010) 1–31.

[12] C. E. K. Iii, L. Chen, Computer simulation of 3-D grain growth using a phase- field model, Acta Materiala 50 (2002) 3057–3073.

[13] M. Elsey, S. Esedoglu, P. Smereka, Simulations of anisotropic grain growth: Efficient algorithms and misorientation distributions, Acta Materialia 61 (6) (2013) 2033–2043. doi:10.1016/j.actamat.2012.12.023.
URL http://dx.doi.org/10.1016/j.actamat.2012.12.023

[14] H. Hallberg, Influence of anisotropic grain boundary properties on the evolution of grain boundary character distribution during grain growth - A 2D level set study, Modelling and Simulation in Materials Science and Engineering 22 (8) (2014). doi:10.1088/0965-0393/22/8/085005.

[15] S. Esedoglu, F. Otto, Threshold Dynamics for Arbitrary Surface Tensions, Comm Pure Appl Math 68 (5) (2015) 808–864. doi:10.1002/cpa.21527.

[16] C. Mießen, M. Liesenjohann, L. A. Barrales-Mora, L. S. Shvindlerman, G. Gottstein, An advanced level set approach to grain growth - Accounting for grain boundary anisotropy and finite triple junction mobility, Acta Materialia 99 (2015) 39–48. doi:10.1016/j.actamat.2015.07.040.

[17] J. Fausty, N. Bozzolo, D. Pino Muñoz, M. Bernacki, A novel level-set finite element formulation for grain growth with heterogeneous grain boundary energies, Materials and Design 160 (2018) 578–590. doi:10.1016/j.matdes.2018.09.050.
URL https://doi.org/10.1016/j.matdes.2018.09.050

[18] J. Fausty, N. Bozzolo, M. Bernacki, A 2D level set finite element grain coarsening study with heterogeneous grain boundary energies, Applied Mathematical Modelling 78 (2020) 505–518. doi:10.1016/j.apm.2019.10.008.
URL https://doi.org/10.1016/j.apm.2019.10.008

[19] X. Zhang, J. S. Chen, S. Osher, A multiple level set method for modeling grain boundary evolution of polycrystalline materials, Interaction and Multiscale Mechanics 1 (2) (2008) 191–209. doi:10.12989/imm.2008.1.2.191.

URL ftp://www.math.ucla.edu/pub/camreport/cam06-69.pdf%5Cnftp://ftp.math.ucla.edu/pub/camreport/cam06-69.pdf

[20] E. A. Holm, G. N. Hassold, M. A. Miodownik, On misorientation distribution evolution during anisotropic grain growth, Acta Materialia 49 (15) (2001) 2981–2991. doi:10.1016/S1359-6454(01)00207-5.

[21] D. Moldovan, D. Wolf, S. R. Phillpot, A. J. Haslam, Mesoscopic simulation of two-dimensional grain growth with anisotropic grain-boundary properties, Philosophical Magazine A: Physics of Condensed Matter, Structure, Defects and Mechanical Properties 82 (7) (2002) 1271–1297. doi:10.1080/01418610208235672.

[22] M. Upmanyu, G. Hassold, A. Kazaryan, E. Holm, Y. Wang, B. Patton, D. Srolovitz, Boundary Mobility and Energy Anisotropy Effects on Microstructural Evolution During Grain Growth, Interface Science 10 (2/3) (2002) 201–216. doi:10.1023/A:1015832431826.
URL http://link.springer.com/10.1023/A:1015832431826

[23] J. Gruber, D. C. George, A. P. Kuprat, G. S. Rohrer, A. D. Rollett, Effect of anisotropic grain boundary properties on grain boundary plane distributions during grain growth, Scripta Materialia 53 (3) (2005) 351–355. doi:10.1016/j.scriptamat.2005.04.004.

[24] J. Gruber, H. M. Miller, T. D. Hoffmann, G. S. Rohrer, A. D. Rollett, Misorientation texture development during grain growth. Part I: Simulation and experiment, Acta Materialia 57 (20) (2009) 6102–6112. doi:10.1016/j.actamat.2009.08.036.
URL http://dx.doi.org/10.1016/j.actamat.2009.08.036

[25] A. Mallick, S. Vedantam, Phase field study of the effect of grain boundary energy anisotropy on grain growth, Computational Materials Science 46 (1) (2009) 21–25. doi:10.1016/j.commatsci.2009.01.026.
URL http://dx.doi.org/10.1016/j.commatsci.2009.01.026

[26] E. Miyoshi, T. Takaki, Extended higher-order multi-phase-field model for three-dimensional anisotropic-grain-growth simulations, Computational Materials Science 120 (2016) 77–83. doi:10.1016/j.commatsci.2016.04.014.
URL http://dx.doi.org/10.1016/j.commatsci.2016.04.014

[27] K. Chang, L. Q. Chen, C. E. Krill, N. Moelans, Effect of strong nonuniformity in grain boundary energy on 3-D grain growth behavior: A phase-field simulation study, Computational Materials Science 127 (2017) 67–77. doi:10.1016/j.commatsci.2016.10.027.
URL http://dx.doi.org/10.1016/j.commatsci.2016.10.027

[28] H. K. Kim, S. G. Kim, W. Dong, I. Steinbach, B. J. Lee, Phase-field modeling for 3D grain growth based on a grain boundary energy database, Modelling and Simulation in Materials Science and Engineering 22 (3) (2014). doi:10.1088/0965-0393/22/3/034004.

[29] J. D. Niño, O. K. Johnson, Influence of grain boundary energy anisotropy on the evolution of grain boundary network structure during 3d anisotropic grain growth, Computational Materials Science 217 (2023) 111879. doi:https://doi.org/10.1016/j.commatsci.2022.111879.
URL https://www.sciencedirect.com/science/article/pii/S0927025622005900

[30] H. Salama, J. Kundin, O. Shchyglo, V. Mohles, K. Marquardt, I. Steinbach, Role of inclination dependence of grain boundary energy on the microstructure evolution during grain growth, Acta Materialia 188 (2020) 641–651. doi:10.1016/j.actamat.2020.02.043.

[31] H. Hallberg, V. V. Bulatov, Modeling of grain growth under fully anisotropic grain boundary energy, Modelling and Simulation

in Materials Science and Engineering (2019). doi:10.1088/1361-651X/ab0c6c.
URL https://doi.org/10.1088/1361-651X/ab0c6c

[32] Read-Shockley, Dislocation Models of crystal grain boundaries, Physical review (1950).

[33] H.-K. Kim, W.-S. Ko, H.-J. Lee, S. G. Kim, B.-J. Lee, An identification scheme of grain boundaries and construction of a grain boundary energy database, Scripta Materialia 64 (12) (2011) 1152–1155.

[34] D. L. Olmsted, S. M. Foiles, E. A. Holm, Survey of computed grain boundary properties in face-centered cubic metals: I. grain boundary energy, Acta Materialia 57 (13) (2009) 3694–3703.

[35] S. G. Baird, E. R. Homer, D. T. Fullwood, O. K. Johnson, Five degree-of-freedom property interpolation of arbitrary grain boundaries via voronoi fundamental zone framework, Computational Materials Science 200 (2021) 110756. doi:https://doi.org/10.1016/j.commatsci.2021.110756.
URL https://www.sciencedirect.com/science/article/pii/S0927025621004833

[36] K. Pawlik, Determination of the orientation distribution function from pole figures in arbitrarily defined cells, Physica status solidi (b) 134 (2) (1986) 477–483.

[37] L. S. Tóth, P. Van Houtte, et al., Discretization techniques for orientation distribution functions, Texture, Stress, and Microstructure 19 (1992) 229–244.

[38] H. J. Bunge, Texture Analysis in Materials Science: Mathematical Methods, 3rd Edition, Cuvillier, 1993.

[39] M. H. Alvi, S. Cheong, J. Suni, H. Weiland, A. Rollett, Cube texture in hot-rolled aluminum alloy 1050 (aa1050)—nucleation and growth behavior, Acta materialia 56 (13) (2008) 3098–3108.

[40] N. Bozzolo, N. Dewobroto, T. Grosdidier, F. Wagner, Texture evolution during grain growth in recrystallized commercially pure titanium, Materials Science and Engineering: A 397 (1-2) (2005) 346–355.

[41] M. T. Pérez-Prado, O. A. Ruano, Texture evolution during grain growth in annealed mg az61 alloy, Scripta Materialia 48 (1) (2003) 59–64.

[42] N. Ma, A. Kazaryan, S. Dregia, Y. Wang, Computer simulation of texture evolution during grain growth: effect of boundary properties and initial microstructure, Acta Materialia 52 (13) (2004) 3869–3879.

[43] D. Zöllner, I. Zlotnikov, Modelling texture dependent grain growth by 2d potts model simulations: A detailed analysis, Computational Materials Science 155 (2018) 180–196.

[44] A. Brahme, J. Fridy, H. Weiland, A. D. Rollett, Modeling texture evolution during recrystallization in aluminum, Modelling and Simulation in Materials Science and Engineering 17 (1) (2008) 015005.

[45] O. Ivasishin, S. Shevchenko, N. Vasiliev, S. Semiatin, 3d monte-carlo simulation of texture-controlled grain growth, Acta materialia 51 (4) (2003) 1019–1034.

[46] N. M. Hwang, B. J. Lee, C. H. Han, Texture evolution by grain growth under a system of anisotropic grain boundary energy, Scripta Materialia 37 (11) (1997) 1761–1767. doi:10.1016/S1359-6462(97)00321-7.

[47] X. K. Lu, S. Yang, Simulating effects of texture on grain boundary character distribution during grain growth, Materials Research Innovations 19 (April) (2015) S267–S271. doi:10.1179/1432891715Z.0000000001557.

[48] B. L. Adams, S. R. Kalidindi, D. T. Fullwood, Microstructure-Sensitive Design for Performance Optimization (1st ed.). Butterworth-Heinemann., 2012. doi:10.1016/C2011-0-07501-4.

[49] M. Knezevic, S. R. Kalidindi, R. K. Mishra, Delineation of first-order closures for plastic properties requiring explicit consideration of strain hardening and crystallographic texture evolution, International Journal of Plasticity 24 (2) (2008) 327–342.

[50] D. Li, H. Garmestani, B. Adams, A texture evolution model in cubic-orthotropic polycrystalline system, International journal of plasticity 21 (8) (2005) 1591–1617.

[51] J. B. Shaffer, M. Knezevic, S. R. Kalidindi, Building texture evolution networks for deformation processing of polycrystalline fcc metals using spectral approaches: Applications to process design for targeted performance, International Journal of Plasticity 26 (8) (2010) 1183–1194.

[52] O. K. Johnson, C. Kurniawan, An efficient algorithm for generating diverse microstructure sets and delineating properties closures, Acta Materialia 147 (2018) 313–321.

[53] M. Huang, J. Jiang, Y. Wang, Y. Liu, Y. Zhang, J. Dong, G. Xiao, Deformation behavior, microstructure evolution, phase transformation and plastic instability origin of powder metallurgy al0.8co0.5cr1.5cufeni alloy during high temperature deformation, Materials Science and Engineering: A 861 (2022) 144373. doi:https://doi.org/10.1016/j.msea.2022.144373.
URL https://www.sciencedirect.com/science/article/pii/S0921509322017531

[54] H. Wang, Y. An, X. Xu, X. Guo, Y. Hu, Rapid solidification microstructure evolution and grain refinement of deeply undercooled nickel alloys, Materials Characterization 170 (2020) 110703. doi:https://doi.org/10.1016/j.matchar.2020.110703.
URL https://www.sciencedirect.com/science/article/pii/S1044580320321744

[55] B. H. S. Madavali, Enhanced thermoelectric properties of p-type bi0.5sb1.5te3 thermoelectric materials by mechanical alloying and spark plasma sintering, J. Electron. Mater. 45 (2016) 110703. doi:https://doi.org/10.1007/s11664-016-5011-6.

[56] O. K. Johnson, C. A. Schuh, Texture mediated grain boundary network design in two dimensions, Journal of Materials Research 31 (2016) 1171–1184.

[57] O. K. Johnson, C. A. Schuh, Texture mediated grain boundary network design in three dimensions, Mechanics of Materials 118 (2018) 94–105.

[58] F. Bachmann, R. Hielscher, H. Schaeben, Texture analysis with mtex–free and open source software toolbox, Solid state phenomena 160 (2010) 63–68.

[59] MTEX Toolbox, "Wigner Functions.", https://mtex-toolbox.github.io/WignerFunctions.html.

[60] B. L. Adams, A. Henrie, B. Henrie, M. Lyon, S. R. Kalidindi, H. Garmestani, Microstructure-sensitive design of a compliant beam, Journal of the Mechanics and Physics of Solids 49 (8) (2001) 1639–1663. doi:10.1016/S0022-5096(01)00016-3.

[61] J. K. Mason, O. K. Johnson, Convergence of the hyperspherical harmonic expansion for crystallographic texture., Journal of Applied Crystallography (2013). doi:10.1107/S0021889813022814.

[62] G. Nolze, R. Hielscher, Orientations – perfectly colored, Journal of Applied Crystallography 49 (5) (2016) 1786–1802. doi:10.1107/S1600576716012942.
URL https://doi.org/10.1107/S1600576716012942

[63] C. Herring, Chapter 8 in the physics of powder metallurgy, MacGraw-Hill, New-York (1951) 143.

[64] J. D. Niño, O. K. Johnson, Study of the evolution of the crystallographic texture and the

grain boundary network of the microstructure during grain growth: Supplemental data (2024). doi:10.17632/rw5b9k847w.1.

[65] M. E. Frary, C. A. Schuh, Correlation-space description of the percolation transition in composite microstructures, Physical Review E - Statistical, Nonlinear, and Soft Matter Physics 76 (4) (2007). doi:10.1103/PhysRevE.76.041108.

[66] M. Frary, C. A. Schuh, Grain boundary networks: Scaling laws, preferred cluster structure, and their implications for grain boundary engineering, Acta Materialia 53 (16) (2005) 4323–4335. doi:https://doi.org/10.1016/j.actamat.2005.05.030.
URL https://www.sciencedirect.com/science/article/pii/S1359645405003319

[67] J. K. Mason, C. A. Schuh, Correlated grain-boundary distributions in two-dimensional networks, Acta Crystallographica Section A 63 (4) (2007) 315–328. doi:10.1107/S0108767307021782.
URL https://doi.org/10.1107/S0108767307021782

[68] J. J. Bhattacharyya, S. Agnew, G. Muralidharan, Texture enhancement during grain growth of magnesium alloy az31b, Acta Materialia 86 (2015) 80–94.

[69] J. K. Mason, C. A. Schuh, Correlated grain-boundary distributions in two-dimensional networks, Acta Crystallographica Section A: Foundations of Crystallography 63 (4) (2007) 315–328.